ARTICLES

Rain, winds and haze during the Huygens probe's descent to Titan's surface

M. G. Tomasko[1], B. Archinal[2], T. Becker[2], B. Bézard[3], M. Bushroe[1], M. Combes[3], D. Cook[2], A. Coustenis[3], C. de Bergh[3], L. E. Dafoe[1], L. Doose[1], S. Douté[4], A. Eibl[1], S. Engel[1], F. Gliem[5], B. Grieger[6], K. Holso[1], E. Howington-Kraus[2], E. Karkoschka[1], H. U. Keller[6], R. Kirk[2], R. Kramm[6], M. Küppers[6], P. Lanagan[1], E. Lellouch[3], M. Lemmon[7], J. Lunine[1,8], E. McFarlane[1], J. Moores[1], G. M. Prout[1], B. Rizk[1], M. Rosiek[2], P. Rueffer[5], S. E. Schröder[6], B. Schmitt[4], C. See[1], P. Smith[1], L. Soderblom[2], N. Thomas[9] & R. West[10]

The irreversible conversion of methane into higher hydrocarbons in Titan's stratosphere implies a surface or subsurface methane reservoir. Recent measurements from the cameras aboard the Cassini orbiter fail to see a global reservoir, but the methane and smog in Titan's atmosphere impedes the search for hydrocarbons on the surface. Here we report spectra and high-resolution images obtained by the Huygens Probe Descent Imager/Spectral Radiometer instrument in Titan's atmosphere. Although these images do not show liquid hydrocarbon pools on the surface, they do reveal the traces of once flowing liquid. Surprisingly like Earth, the brighter highland regions show complex systems draining into flat, dark lowlands. Images taken after landing are of a dry riverbed. The infrared reflectance spectrum measured for the surface is unlike any other in the Solar System; there is a red slope in the optical range that is consistent with an organic material such as tholins, and absorption from water ice is seen. However, a blue slope in the near-infrared suggests another, unknown constituent. The number density of haze particles increases by a factor of just a few from an altitude of 150 km to the surface, with no clear space below the tropopause. The methane relative humidity near the surface is 50 per cent.

The surface of Titan has long been studied with various instruments, including those on the Hubble Space Telescope (HST) and ground-based adaptive optics systems[1]. More recently, Cassini investigations using the charge-coupled device (CCD) camera[2], the Visible and Infrared Mapping Spectrometer (VIMS) instrument[3], and the Radio Detection and Ranging (RADAR) imaging system[4] have provided more detailed views of Titan's surface in the hope of revealing how the methane in Titan's atmosphere is replenished from the surface or interior of Titan. Of the Cassini imagers, the Imaging Science Subsystem (ISS) camera is potentially capable of the greatest spatial resolution, but Titan's obscuring haze limits its resolution on the surface to about 1 km, a value roughly similar to that available from VIMS and the radar imaging system. At this resolution, the bright and dark regions observed on the surface of Titan have proved difficult to interpret. Owing to its proximity to the surface, the Descent Imager/Spectral Radiometer (DISR) camera on the Huygens probe was capable of a linear resolution of some metres from a height of 10 km. In addition, the lower the probe descended, the less haze lay between the camera and the ground. The DISR was capable of linear resolution orders of magnitude better than has been available from orbit, although of a much smaller portion of Titan's surface. Also, a lamp was used at low altitude to measure the continuous reflectance spectrum of the surface without the complications introduced by observations through large amounts of methane and aerosol haze[5].

In addition to studying the surface of Titan, the DISR took measurements of solar radiation in the atmosphere. Spectrometers looking upward at continuum wavelengths (between the major methane absorptions) as well as downward measured the vertical distribution and wavelength dependence of the aerosol haze opacity. Measurements of the polarization of light at a scattering angle of 90° constrained the small dimension of the haze particles. Measurements of the brightness in the solar aureole around the Sun determined the projected area of the haze particles. Observations in the methane bands determined the methane mole fraction profile.

Data collection during the descent proceeded mostly, although not exactly, as planned. Turbulence during the first half of the descent tipped the probe more rapidly than expected, causing the Sun sensor to remain locked on the azimuth of the Sun for only a few successive rotations at a time. Below about 35 km, the signal from the direct solar beam was lost by the Sun sensor owing to the unexpectedly low temperature of this detector. These effects caused data from each of the DISR sub-instruments to be collected at mostly random, instead of specific, azimuths. Additionally, the probe rotated in the intended direction for only the first ten minutes before rotating in the opposite sense for the remainder of the descent. This resulted in ineffective baffling of the direct solar beam for the upward-looking visible spectrometer and the solar aureole camera. Consequently, some measurements made by the solar aureole camera are saturated, and the separation of the direct and diffuse solar beams in the visible spectral measurements must be postponed until a good model of the probe attitude versus time is available. Finally, the loss of one of

the two radio communication channels in the probe receiver aboard the orbiter resulted in the loss of half the images as well as several other low-altitude spectrometer measurements.

Despite these misfortunes, the DISR instrument collected a unique and very useful data set. Images of the surface with unprecedented resolution were collected over the boundary between bright and dark terrain seen from the orbiter. Owing to redundant transmission over both communication channels during most of the descent, almost all of the spectral and solar aureole observations were received. A very large set of high-quality spectra were obtained with good altitude resolution and with good coverage in azimuth both away from and towards the Sun. The images, the spectra, the Sun sensor pulses, the recording of the gain in the Cassini radio receiver, and information from Very Long Baseline Interferometry (VLBI) observations from Earth together will permit reconstruction of the probe attitude relative to the Sun as a function of time during the descent, enabling

a full analysis of the spectral data. The large number of solar aureole measurements included several acquired near the Sun and many polarization measurements opposite to the Sun. The surface science lamp worked exactly as planned, permitting surface reflection measurements even in strong methane absorption bands. Operations after landing included the collection of successive images as well as spectral reflectance measurements of the surface illuminated by the lamp from an assumed height of roughly 30 cm.

Taken together, the new observations shed substantial light on the role played by methane in forming the surface of Titan and how it is recycled into the atmosphere. The substantial relative humidity of methane at the surface and the obvious evidence of fluid flow on the surface provide evidence for precipitation of methane onto the surface and subsequent evaporation. Some indications of cryovolcanic flows are also seen. The vertical distribution and optical properties of Titan's haze have been characterized to aid the interpretation of remote measurements of the spectral reflection of the surface. The speed and direction of Titan's winds has also been measured for comparison with future dynamical models that include the radiative heating and cooling rates implied by the haze.

Physical processes that form the surface

The imagers provided views of Titan's previously unseen surface, thus allowing a deeper understanding of the moon's geology. The three DISR cameras were designed to provide overlapping coverage for an unbroken 360°-wide swath stretching from nadir angles between 6° and 96°. Some 20 sets of such images were planned during the descent. Because of the opacity of the haze in the passband of our imager, surface features could be discerned in the images only below about 50 km, limiting the number of independent panoramic mosaics that can be made of the surface. The loss of half of the images meant that Titan's surface was not covered by systematic overlapping triplets, as expected. Three different views of Titan's surface are
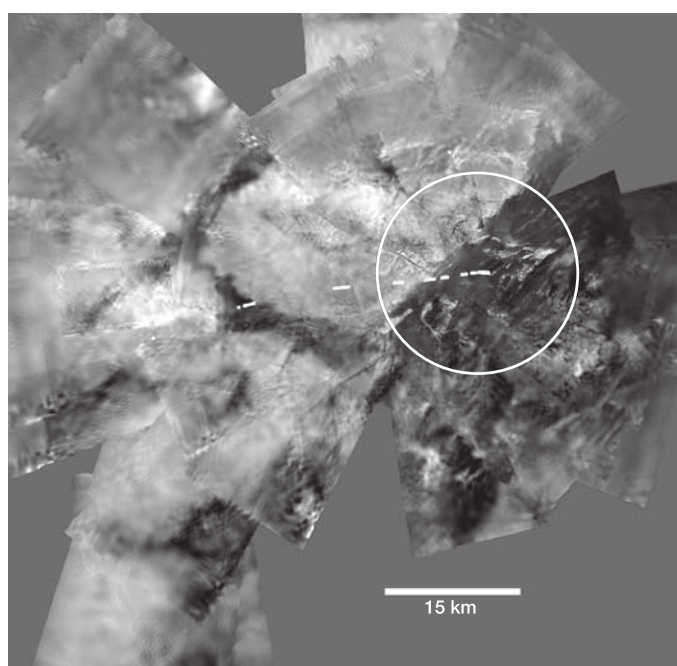

Figure 1 | **View of Titan from 34 km above its surface.** High-altitude (49 to 20 km) panoramic mosaic constructed from the DISR High and Medium Resolution Imagers (HRI and MRI) as projected from 34 km. The preliminary ground-track solution (indicated as small white points on gnomonic ground projection) represents the location of the probe when data were collected; north points up; scale indicated (although subsequent analysis indicates that north lies some 5–10° to the left of straight up in this and the two subsequent figures). Starting from the first surface image at 49 km, the probe moves in an east-northeastwardly direction at an initial speed of 20 m s^{-1}. Brighter regions separated by lanes or lineaments of darker material are seen. No obvious crater-like features are visible. The circle indicates the outline of the next-lowest pan, in Fig. 2. The method used for construction of panoramic mosaics incorporates knowledge of the probe's spatial location (longitude, latitude and altitude) and attitude (roll, pitch and yaw) at each image. With the exception of altitude, provided by the Huygens Atmospheric Structure Instrument[12] pressure sensor, none of these variables was directly measured. They are found through an iterative process in which a panorama is created, providing an improved ground-track and azimuth model, which results in an upgraded trajectory, which can improve the panorama, and so on. The current lack of pitch and roll knowledge constitutes the main source of error in the current composition and quality of the panoramas as well as the ground-track and wind speed determination reported below. Vigorous contrast-stretching in the images is required to reveal details washed out by the haze particle density at all altitudes in Titan's atmosphere. This contrast-stretching also displays the occasional ringing of the Discrete Cosine Transform data compressor, which appear as regular lines of bright and dark patterns, particularly in the MRI images.
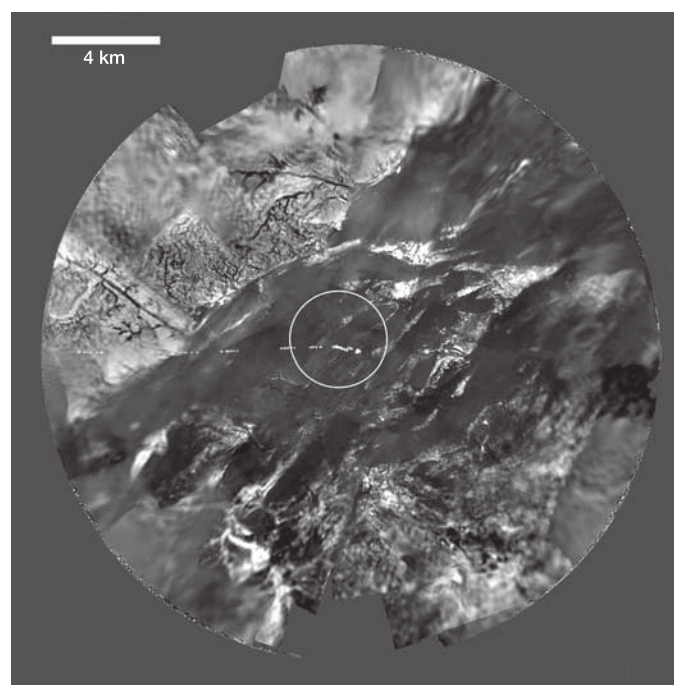

Figure 2 | **View from 8 km.** Medium-altitude (17 to 8 km) panoramic mosaic projected from 8 km. As in Fig. 1, the preliminary ground-track solution is indicated as points; north is up; scale indicated. At 11 km, the wind direction is at 0° (eastward), reaching −20° (southeastward) at an altitude of 8.5 km. The narrow dark lineaments, interpreted as channels, cut brighter terrain. The circle indicates the outline of the low-altitude pan in Fig. 3.

shown in Figs 1 to 3. A view of Titan's surface after the Huygens landing is shown in Fig. 4.

The highest view (Fig. 1), projected from an altitude of 34 km, displays an albedo variation very similar to the highest-resolution images provided by the ISS or VIMS cameras on the Cassini orbiter. It shows Titan's surface to consist of brighter regions separated by lanes or lineaments of darker material. No obvious impact features are visible, although craters less than roughly 10 km should not be abundant as a result of atmospheric shielding[6]. In the rightmost (eastern) part of the mosaic the images become sharper as the lower altitude of the camera causes the scale to decrease and the contrast to increase. More than a dozen brighter areas in that region seem to be elongated along a direction parallel with the main bright/dark boundary of that region. At the limit of resolution, narrow dark channels cut the bright terrain.

The next view, Fig. 2, projected from an altitude of 8 km, reveals a large number of these channels (detailed in Fig. 5). The channel networks have two distinct patterns: short stubby features and dendritic features with many branches. The region of the stubby network towards the west is significantly brighter than the dendritic region. The stubby channels are shorter, wider and relatively straight. They are associated with and often begin or end in dark circular areas, which suggest ponds or perhaps pits. The morphology of rectilinear networks with stubby heads is consistent with spring-fed channels or arroyos.

The dendritic network is consistent with rainfall drainage channels, implying a distributed rather than a localized source of a low-viscosity liquid. Stereo analysis of the dendritic region indicates an elevation of 50–200 m relative to the large darker plain to the south. It suggests that the brighter areas within the darker terrain are higher as well. The topographic differences are evident in Figs 6 and 7, which are three-dimensional renderings of the area just north of the landing site produced from the DISR images. They include the major bright–dark interface seen from above in Fig. 5. Figure 2 depicts many examples of these darker lanes of material between topographically higher, brighter areas. In fact the low contrast of the lowland plane argues that the entire dark region floods, and as the liquid drains the local topography drives flows as seen in the images. If the darker region is interpreted as a dried lakebed, it is too large to have been caused by the creeks and channels visible in the images. It may have been created by other larger river systems or some large-scale catastrophic event, which predates deposition by the rivers seen in these images.

The interpretation of the dark lanes within the brighter highlands as drainage features is so compelling as to dominate subsequent interpretation of other areas of images such as Figs 2 and 3. The prevailing bright–dark boundary of the region becomes a coastline, the bright areas separated from this boundary become islands. Bright streaks running parallel to the albedo boundary may be drift deposits or splays fractured off the bright highlands owing to faulting along the shoreline.

When coupled with Fig. 4, which is an image of a typical offshore dark region, it is clear that the analogy has a limit. At present there is no liquid in the large dark lakebed imaged in Figs 1 to 5. The bright lobate feature, split by an apparently straight dark lane in the western part of the mosaic in Fig. 2, is a possible fissure-fed cryovolcanic flow. However, Fig. 4 also reveals rocks which—whether made of silicates or, more probably hydrocarbon-coated water-ice—appear to be rounded, size-selected and size-layered as though located in the bed of a stream within the large dark lakebed. Rounded stones approximately 15 cm in diameter and probably composed of water-ice, lie on top of a darker, finer-grained surface.
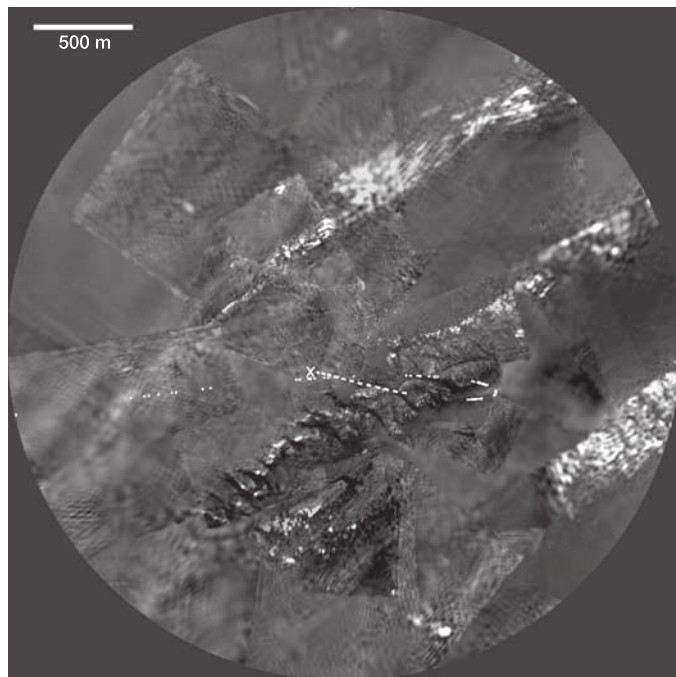

Figure 3 | View from 1.2 km. Low-altitude (7 to 0.5 km) panoramic mosaic projected from 1,200 m. As in Figs 1 and 2, the preliminary ground track is indicated as points; north is up; scale indicated. The probe's steady east-northeast drift halts altogether at an altitude of 7 km and reverses, moving west-northwest for some 1 km during the last 15 min of descent. Note the ridge near the centre, cut by a dozen darker lanes or channels. The projected landing site is marked with an 'X' near the continuation of one of the channels, whose direction matches the orientation of the stream-like clearing in the near-foreground of the southward-looking surface image, Fig. 4.
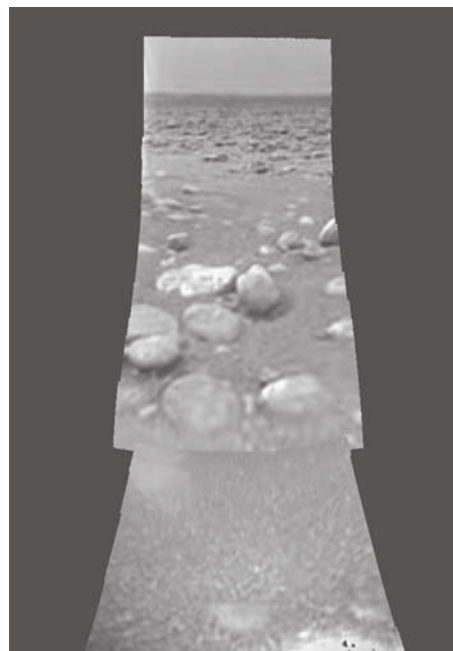

Figure 4 | The view from Titan's surface. Merged MRI and SLI images acquired after the Huygens probe soft-landing. Horizon position implies a pitch of the DISR nose upward by $1.7 \pm 0.2°$ with no measurable roll. 'Stones' 10–15 cm in size lie above darker, finer-grained substrate in a variable spatial distribution. Brightening of the upper left side of several rocks suggests solar illumination from that direction, implying a southerly view, which agrees with preliminary evidence from other data sets. A region with a relatively low number of rocks lies between clusters of rocks in the foreground and the background and matches the general orientation of channel-like features in the low-altitude pan of Fig. 3. The bright spot in the lower right corner is the illumination of the DISR surface science lamp.

It is interesting to compare the brightness and colour of the scene shown in Fig. 4 with that of a similar scene on the Earth. The brightness of the surface of the Earth illuminated by full sunlight is about half a million times greater than when illuminated by a full moon. The brightness of the surface of Titan is about a thousand times dimmer than full solar illumination on the Earth (or 500 times brighter than illumination by full moonlight). That is, the illumination level is about that experienced about 10 min after sunset on the Earth. The colour of the sky and the scene on Titan is rather orange due to the much greater attenuation of blue light by Titan's haze relative to red light. If the Sun is high in the sky, it is visible as a small, bright spot, ten times smaller than the solar disk seen from Earth, comparable in size and brightness to a car headlight seen from about 150 m away. The Sun casts sharp shadows, but of low contrast, because some 90% of the illumination comes from the sky. If the Sun is low in the sky, it is not visible.

The sizes of the more than 50 stones in the image in Fig. 4 vary between 3 mm in diameter, the resolution limit of the imager, and 15 cm. No rocks larger than 15 cm are seen. The resolution of the last images taken before landing from a height of 200–300 m would be sufficient to identify metre-sized objects, and none are seen in the 40×35 m field of view. Figure 8 shows the R value, a measure of the fraction of the surface covered by rocks of a given size frequently used to describe the size distribution of impact craters or crater ejecta. A larger fraction of the surface is covered with rocks greater than 5 cm as opposed to smaller pebbles. The dominance of the cobbles 5–15 cm in size suggests that rocks larger than ~15 cm cannot be transported to the lakebed, while small pebbles (<5 cm) are quickly removed from the surface. Figure 8 confirms the visual impression given by Fig. 4 that the surface coverage of rocks in the foreground of the image (<80 cm horizontal distance from the probe) is higher than in the region beyond (about 80–160 cm). However, this trend is not seen for the pebbles less than 5 cm in size.

Elongated dark trails aligned with the general trend of the possible stream-bed visible in the centre of Fig. 4 extend from several of the distant boulders. The direction of the trails agrees with the general northwest–southeast alignment of the stream-like features shown in Fig. 3, because the last upward-looking spectra indicate that the probe settled with DISR facing southward. Images taken from the surface show no traces of the landing of the probe. The viewing direction is probably generally not downwind (the parachute is not visible).

When coupled with the shapes, size selection and layering of the stones in Fig. 4, the elongated islands and their orientation parallel to the coastline in Fig. 1, the stubby and dendritic channel networks, as well as the ponds in Fig. 2 and Fig. 5, the major elements of the Titan surface albedo variations can be interpreted to be controlled by flow of low-viscosity fluids driven by topographic variation, whether caused by precipitation (the dendritic networks) or spring-fed flows (the stubby networks). We thus interpret the bright–dark albedo difference as follows: irrigation of the bright terrain results in darker material being removed and carried into the channels, which discharge it into the region offshore, thereby darkening it. Eolian processes such as wind gusts coupled with Titan's low gravity (compared to Earth) may aid this migration.

The dark channels visible in the lowest panorama (Fig. 3) seem to suggest south-easterly fluid flow across the lower plane, depositing or exposing the brighter materials (water ice?) along the upstream faces of the ridges.

Stereographic rendering of the dendritic channels just north of the probe landing site (Figs 6 and 7) shows that the slopes in bright terrain being dissected by the putative methane river channels are
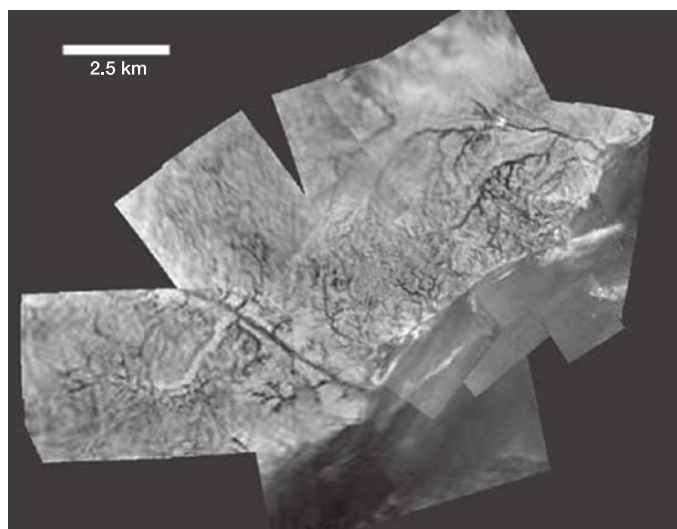

Figure 5 | View of 'shoreline' and channels. Panoramic mosaic projected from 6.5 km. showing expanded view of the highlands and bright-dark interface. As in previous figures, north is up; scale indicated. Branching and rectilinear channel networks of dark lanes are shown along an albedo boundary approximately 12 km long.
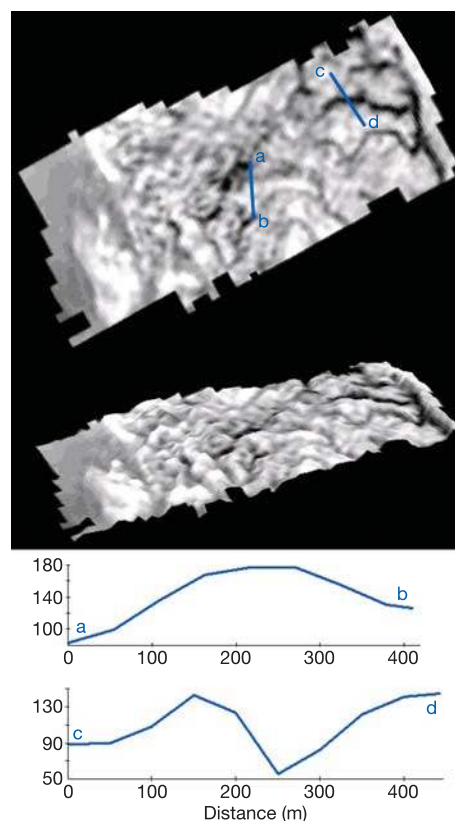

Figure 6 | Topographic model of highland region ~5 km north of the Huygens landing site. The top panel shows an orthorectified HRI image from stereo pair (vertical view). The middle panel shows a perspective view of the topographic model with ~50° tilt angle. No vertical exaggeration was applied (it is 1:1). The bottom panel shows profiles (a–b and c–d from the top panel) that illustrate the extremely steep topography in the region dissected by the drainages. All dimensions are in metres. A DISR stereo pair (using HRI frame 450 and MRI frame 601) was photogrammetrically analysed using a digital stereo workstation. The overlapping area of stereo coverage is about 1×3 km; the convergence angle is ~25°. The coincidence of the drainage patterns with the valley floors gives confidence in the reality of the topographic model; the height accuracy is ~20 m. This preliminary model has been arbitrarily levelled so that the elevation differences are only relative.

extremely rugged; slopes of the order of 30° are common. This suggests relatively rapid erosion by flows in the river beds, resulting in the deeply incised valleys. Erosion by steep landslides on slopes approaching the angle of repose is probably the primary mechanism by which the rugged topography is formed. Figure 7 shows two stereographic views of the shoreline and hillside north of the landing site.

The wind profile

Assembly of the panoramic mosaics leads to the construction of a descent trajectory as part of an iterative process of image reconstruction. The trajectory can be used to derive the probe ground track and extract the implied wind velocity as a function of altitude. Correlation of the roughly 200 usable images acquired by DISR during its descent resulted in longitude and latitude values versus time, displayed in Fig. 9. Fitted by polynomials, these ground tracks were differentiated with respect to time and scaled to derive the horizontal wind speed and direction as functions of altitude.

The results indicate that the probe's steadily increasing eastward drift caused by Titan's prograde winds, as shown in Fig. 10, slowed from near 30 to $10 \, m \, s^{-1}$ between altitudes of 50 and 30 km and slowed more rapidly (from 10 to $4 \, m \, s^{-1}$) between altitudes of 30 and 20 km. The winds drop to zero and reverse at around 7 km, near the expected top of the planetary boundary layer, producing a west-northwestwardly motion extending for about 1 km during the last 15 min of the descent (see Fig. 3). The generally prograde nature of the winds between 50 and 10 km agrees with models of Titan's zonal winds available before the arrival of Cassini or the Huygens probe[7], although the wind speed is somewhat less than the average predicted before entry.

The planetary boundary layer is calculated to have a thickness of between 4 and 8 km, based on scaling the Earth's near-equatorial planetary-boundary-layer thickness of 1–2 km by the inverse square-rooted ratio of the planetary rotation rates. The minimum horizontal wind speed at 7 km can thus be an indication of entry into the boundary layer[8]. The reversal of wind direction at this altitude is also consistent with the Voyager-derived equatorial temperature profile[9], wherein the temperature gradient changes from dry adiabatic to a sub-adiabatic temperature gradient above 4 km altitude, indicating the top of the boundary layer.

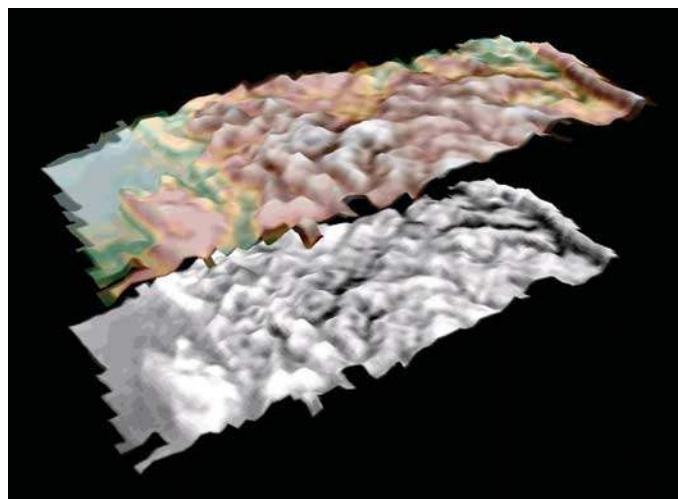The current ground-track and wind-speed analysis predicts

winds of about 0.3 to $1 \, m \, s^{-1}$ near the surface. This velocity can be produced by any number of sources including pressure and temperature gradients and tides[10].

Migration of surface material

The acquisition of visible spectra at known locations in the images allowed correlation of the reflectance spectra with different types of terrain. The Downward-Looking Visible Spectrometer (DLVS) was an imaging spectrometer measuring light between 480 and 960 nm as it projected the image of the slit onto the ground into up to 20 spatial resolution elements for nadir angles from 10° to 50°. Spectra were collected at nominally the same azimuths as the images, though often at slightly different altitudes (on different probe rotations). Interpolation between the times at which the spectral and image data were obtained located the spectra within the images. Determination of the surface reflectivity was hindered by scattering from the haze between the camera and the surface as well as by methane absorption. Correlation of the spectra with images was therefore best performed on measurements during which the altitude changed only slightly.

The centre of the image in Fig. 11 is displayed in true colour (that is, as the human eye would see it under Titan's atmosphere) using actual spectral data from one panorama. The area between the spectra is interpolated in azimuth. The coverage with spectra is similar to that shown in Fig. 12. The orange colour is due mainly to the illumination of the surface. Scattering and absorption (which dominate in the blue) cause the perceived true colour of the surface to change from yellow to orange with decreasing altitude. Note that the passband of the cameras peaked in the near infrared (at 750 nm), and therefore the brightness variations in the images would not necessarily be seen by the human eye.

In Fig. 12 the images are correlated with the ratio of the intensity in two methane windows (827 nm/751 nm) located in the infrared part of the spectrum where scattering is minimal and the systematic variability with nadir angle can be ignored. Reddening (high 827 nm/ 751 nm ratio) is concentrated at the area covered with drainage

Figure 7 | Titan's surface. Perspective view of Titan's surface using a topographic model of the highland region ~5 km north of the Huygens probe landing site derived from the DISR images. The model in greyscale and false colour shows the elevation (pale white highest). The lowland plane or lakebed is to the left side of the display (in blue); the northern highlands (with the dendritic channels) is to the right.
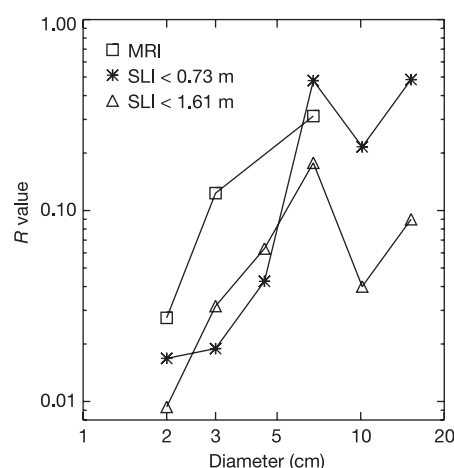

Figure 8 | Distribution of rock on the surface. Rocks larger than 1.63 cm as an R-plot, frequently used to describe size distribution of impact craters or crater ejecta. If N is the number of rocks per centimetre increment of rock size, the fraction of the surface area A covered by rocks with diameters between d and $d + \Delta d$ is approximately $N \times \Delta d \times d^2/A$. By keeping the size bin Δd proportional to the diameter d, the quantity $N \times d^3/A$ (the R value) is also proportional to the surface fraction covered by rocks of diameter d (with a proportionality constant of ~3). The plot shows R values derived from rock counts from the SLI and MRI surface images. For the SLI, R values from counts up to a distance from the probe of 73 cm and up to 161 cm are presented in separate curves. The comparison between the two curves suggests that the count is complete in the displayed size range. The increase of the R value with size corresponds to a higher fraction of the surface covered with large rocks than with smaller ones.

channels (north and northwest in the pan of Fig. 12) and to a lesser degree to the lake area adjacent to the coastline. The lake area in the southeast is not reddened. A preliminary analysis of spectra recorded in other panoramic cycles indicates that the land area in the northeast, which is not covered by drainage channels, is only moderately reddened compared to the river area. The reddening is not restricted to these two methane windows. Figure 13 shows that, in fact, it is present over the whole visual range, amounting to about 6% per 100 nm (note that atmospheric backscatter dominates over surface reflection at wavelengths below 600 nm).

The DLVS data clearly show that the highlands (high-albedo area) are redder than the lakebed (low-albedo area). Spectra of the lakebed just south of the coastline are less red than the highlands but clearly more red than the lakebed further away (that is, to the southeast). The data suggests that the brighter (redder) material of the hilly area may be of local origin, and is corrugated by rivers and drainage channels, and that the darker material (less red) is a substance that seems to be washed from the hills into the lakebed. It could be connected to the alteration of the highland terrain, either by precipitation, wind and/or cryoactivity. Additionally, it could indicate that the surface of the lowland area may be covered by different materials in regions that exhibit diverse morphology.
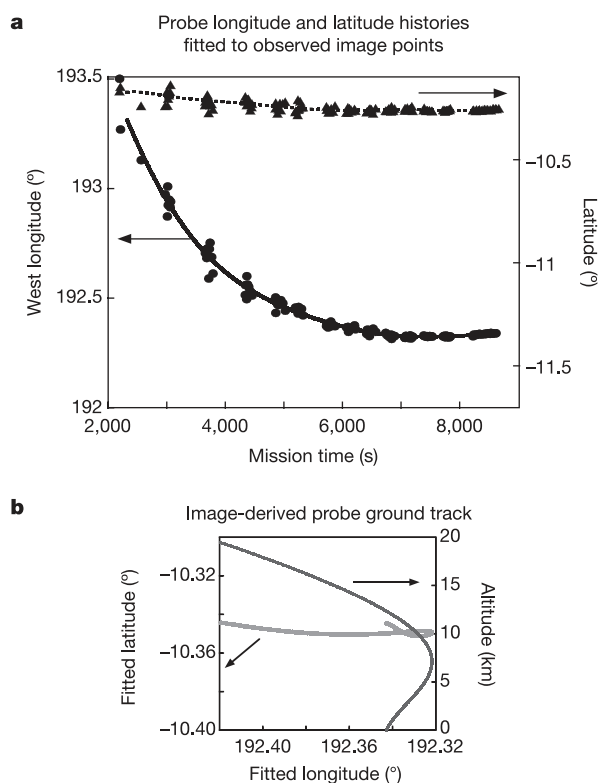

Figure 9 | Probe ground track. a, Sub-probe west longitude and latitude histories of the Huygens probe derived from panoramic image reconstructions. Arrows indicate the appropriate vertical axis. The image data points from which the latitude and longitude were derived are shown as triangles and dots respectively. The dotted and solid lines show polynomial fits to the data. Results adjusted to agree with the Descent Trajectory Working Group (DTWG-3) values at 2,200 s after T_0 (mission time). **b**, Probe longitude versus latitude (thicker line) and versus altitude (thinner line). The altitude axis needs to be expanded by a factor of almost six to recover one-to-one correspondence on a linear scale because the total longitudinal variation is less than 4 km. Using the Doppler Wind Experiment's (DWE) high-altitude references[33], the touchdown point (the predicted landing site) was extrapolated to west longitude 192.34°, latitude −10.34°. Using DTWG-3 high-altitude references, the touchdown point was extrapolated to 192.36°, latitude −10.36°.

Surface reflectivity and methane mole fraction

Spectra taken near Titan's surface allow measurement of its reflectance and determination of the local methane mole fraction. These measurements provide clues as to the make-up of Titan's crust. The Downward-Looking and Upward-Looking Infrared Spectrometers (DLIS and ULIS) cover the region from 840 to 1,700 nm with a resolution of 15 to 20 nm. The ULIS looks up at a half-hemisphere through a diffuser while the DLIS projects its slit into a 3 by 9° field centred at a 20° nadir angle. Below 700 m altitude, a 20-W lamp was turned on to illuminate the surface at wavelengths where solar light had been completely absorbed by methane in Titan's atmosphere. At low altitudes we took repeated DLIS and ULIS spectra at short integration times (1 s). Nine DLIS and seven ULIS spectra were received between 734 and 21 m altitude. The DLIS continued to measure surface spectra free of atmospheric methane absorption after landing. About 20 such identical spectra were acquired from a distance of a few tens of centimetres of the surface.

DLIS spectra at all altitudes clearly showed an additional signal when the lamp was on. However, at the highest altitudes, the lamp reflection from the surface was negligible, so the additional signal was solely due to scattered light from the lamp into the instrument. This scattered light was estimated from the intensity level in the strong methane bands in the highest-altitude spectrum recorded with the lamp on, and removed from all DLIS spectra. After this correction, only spectra at 36 m and especially 21 m showed significant signal from the lamp. This signal dominated the upward intensity due to solar illumination in all regions of strong and moderate methane absorption, while the latter dominated in the methane windows.

This spectrum, which represents the product of the ground reflectivity and the two-way methane transmission, is shown in Fig. 14 and compared to synthetic spectra with methane mole fractions of 3%, 5% and 7%. The ground reflectivity assumed in
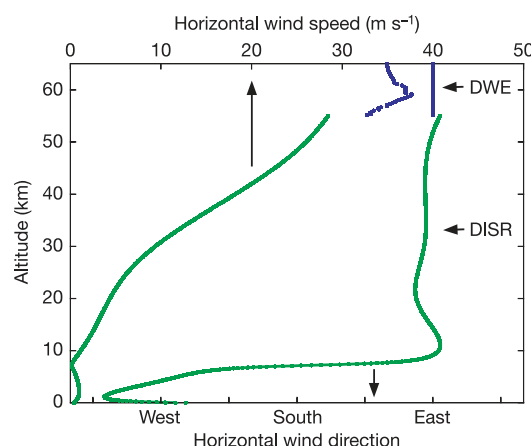

Figure 10 | Observed winds. Horizontal wind speed and direction (counter-clockwise from east) as a function of altitude. The green lines are the DISR data and the blue lines are the high altitude DWE data[33] (showing reasonable consistency between the two). The lines on the left show the wind-speed profile, and on the right is the wind direction. The wind is computed from the combined longitude and latitude reconstructions displayed in Fig. 9. Titan's prograde winds slow from about 28 m s^{-1} at 50 km to 10 m s^{-1} near 30 km altitude, then decrease more rapidly from 30 km (10 m s^{-1}) down to 7 km where they drop to zero. Below 7 km (which is near the expected top of the planetary boundary layer) the winds reverse and become retrograde, and the speed increases to about 1 m s^{-1} around 2–3 km before dropping to almost zero (~0.3 m s^{-1}) near the surface. The direction begins as due east, and then turns through south (beginning between 9–7 km) to the west-northwest between 7–5 km. The winds are extrapolated to be retrograde at the surface, but the two-sigma error bars (not shown) of 1 m s^{-1} at the surface could include surface prograde winds. The error bars at 55 km altitude (4 m s^{-1}) are consistent with continuity from the DWE measurements.

these model calculations is shown in the inset. Four methane bands are seen in the lamp-only spectrum. The good correlation with the models, notably in the weak structures at 1,140, 1,370 and 1,470 nm, indicates a high signal-to-noise ratio of about 50. The best fit is achieved with a methane mole fraction of 5%, which is in firm agreement with the 4.9% *in situ* measurements made by the Gas Chromatograph Mass Spectrometer[11]. Most structures are well reproduced; notable exceptions are the detailed shape of the 1,000 nm band and the absorption shoulder near 1,320 nm.

We conclude that the methane abundance is $5 \pm 1\%$ in the atmosphere near the surface. The corresponding (two-way, and including the 20° lamp inclination) methane column abundance in the spectrum is 9.6 m-amagat (or a column 9.6 m high at the standard temperature and pressure of 273 K and 1 atmosphere). With a temperature of 93.8 K and pressure of 1467.6 mbar (ref. 12), the relative humidity of methane is about 50% using Brown and Ziegler's saturation law[13]. Therefore, methane near the surface is not near saturation, and ground fogs caused by methane in the neighbourhood of the landing site are unlikely.

The ratio of the observed spectrum to the methane transmission, restricted to spectral regions where the latter is higher than 90%, is shown in Fig. 15a ('plus' symbols). It is compared to one of the DLIS spectra after landing, divided by the lamp spectral response and rescaled by a constant reflectivity factor. Note that although this spectrum shows signs of methane absorption at 1,140–1,160 nm and 1,300–1,400 nm, no attempt of correction was made, in the absence so far of accurate information on the absorption path lengths. The agreement between the shapes of the two independent determinations of the ground reflectivity adds confidence to the result.

The four major characteristics of the surface spectrum are: (1) a relatively low albedo, peaking around 0.18 at 830 nm; (2) a red slope in the visible range; (3) a quasilinear decrease of the reflectivity by a factor of about two between 830 and 1,420 nm; and (4) a broad absorption, by ~30% of the local continuum, apparently centred near 1,540 nm (although its behaviour beyond 1,600 nm is poorly constrained) as seen in Fig. 15b. This spectrum is very unusual and has no known equivalent on any other object in the Solar System.

Ground-based spectroscopic observations have provided strong evidence, although spectrally restricted to the methane windows, for the presence of water ice on Titan's surface[14], coexisting in variable proportions with a dark component, presumably of organic nature[15,16]. Water ice may explain the 1,540 nm band, as illustrated in Fig. 15b by a simulation of the reflectance spectrum of a mixture of low-temperature water ice[17], yellow tholins[18] and a spectrally neutral dark component. This identification is reasonable in the context of the light-coloured rocks present at the landing site (Fig. 4), but not conclusive, because some organics do show absorption at a similar wavelength. This is the case, notably, for bright yellow-orange tholins produced in laboratory experiments[19,20] (shown in Fig. 15b), which partly contribute to this band in the simulation and which may account for the red slope in the visible range of the surface spectrum. It is probably this material, existing as aerosol particles, that absorbs the blue wavelengths, which would explain the yellow-orange colour of Titan's atmosphere as seen from space or from the surface.

We note the remarkable absence of other absorption features in the surface spectrum along with the 1,540 nm band. This is at odds with predictions that some specific chemical bonds, in particular C–H or C≡N, and possibly the individual bands of atmospherically abundant species, such as ethane (C_2H_6), acetylene (C_2H_2), propane (C_3H_8), ethylene (C_2H_4), hydrogen cyanide (HCN) and their polymers, would show up as signatures in the surface spectrum.

The most intriguing feature in the surface spectrum is its quasilinear featureless 'blue slope' between 830 and 1,420 nm. As briefly illustrated in Fig. 15b, a featureless blue slope is not matched by any combination of laboratory spectra of ices and complex organics, including various types of tholins. Depending on their composition and structural state (for example, abundance, extension and/or clustering of sp^2 carbon bonds), organic materials in the near-infrared exhibit either distinct absorption bands (for example, bright yellow-orange tholins,
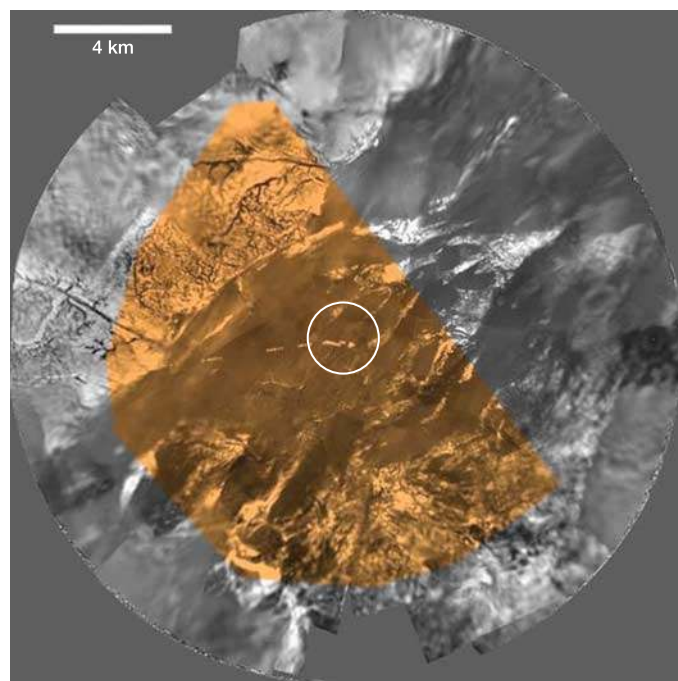

Figure 11 | The surface of Titan displayed in true colour. As seen from an altitude of 8 km. See Fig. 12 for the location of the spectrometer's footprints. Some bright features appear to be overexposed because they are too bright for their colour (the brightness in this image mainly derives from the near-infrared spectrum). True colour is expressed in red-green-blue (RGB) values that are derived by multiplying the spectra with the Commission Internationale de l'Eclairage colour-matching functions (with the 6,500-K correlated colour temperature, the D65 white point). The circle shown is the extent of the lowest panorama (Fig. 3).
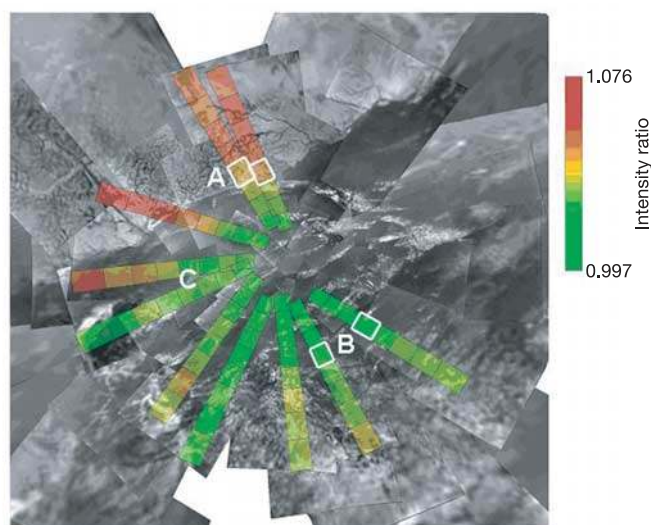

Figure 12 | Reflectivity samples of Titan's surface. A panorama of Titan's surface overlaid with DLVS footprints coloured according to the 827 nm/751 nm intensity ratio, coded from red (high) to green (low). Spectral footprints (the small rectangles) selected for analysis in Fig. 13 are outlined in white. The panorama shows an area of 23 by 23 km. Areas A, B and C are referred to in Fig. 13.

Fig. 15b), or a feature-poor red slope (for medium to low-albedo organics), or a very dark and flat spectrum[18,21].

Assessing the material responsible for the blue slope is a major challenge and also a prerequisite for a secure identification of the 1,540 nm band. If this band is indeed mostly due to water ice, an intimate mixing of this ice with a material displaying a strong 'infrared-blue' absorption would explain the absence of the weaker H_2O bands at 1.04 and 1.25 μm in the surface spectrum, as demonstrated for several dark icy satellites, where these bands are hidden by the presence of an organic component (but neutral or reddish). Decreasing the water-ice grain size alone cannot suppress the 1.04- and 1.25-μm bands and at the same time maintain the apparent blue slope that is produced by large-grained water ice (considering only the continuum absorption between the infrared bands). To hide these weak water bands efficiently, the mixture would need to be ice and a material having a stronger and decreasing-with-wavelength infrared absorption.

Haze particle size

The haze particles in Titan's atmosphere have long been known to produce both high linear polarization and strong forward scattering. This has been taken to imply that the particles are aggregates of small 'monomers' in open structures. The amount of linear polarization constrains the size of the small dimension (monomer radius) while the forward scattering or wavelength dependence of extinction optical depth determines the overall size of the particle or the number of monomers constituting the aggregate.

The DISR instrument measured the degree of linear polarization of scattered sunlight by measuring a vertical strip of sky in two bands centred at 492 and 934 nm. Some 50 measurements of this type were collected during the Titan descent. For the small monomer sizes expected, the direction of polarization would be perpendicular to the scattering plane and reach a maximum near 90° scattering angle at an azimuth opposite to the Sun, and would have a maximum electric field vector in the horizontal direction. We eliminated any polarization measurements made by the DISR that did not have this character, assuming that they were not made at the desired azimuth.
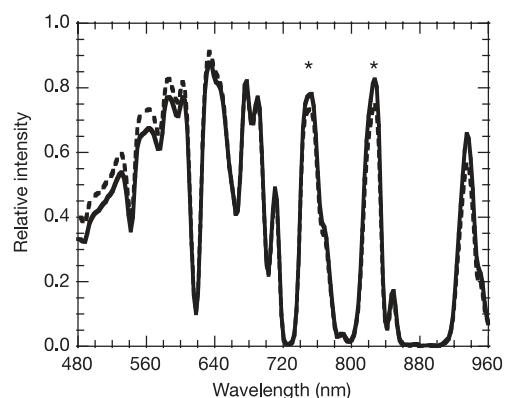
Several polarization measurements showing the expected behaviour in Titan's atmosphere were obtained. A gradual rise to a maximum near a scattering angle of 90° was observed, followed by a decrease on the other side of this peak. The solar aureole camera made several of these measurements at different times through the descent that show a smooth decrease in polarization with increasing optical depth into the atmosphere (Fig. 16). Figure 16a shows a maximum degree of linear polarization of about 60% at altitudes above 120 km in the 934-nm channel. Below, we show that the optical depth at 934 nm is a few tenths at this location in the descent. Comparisons of this degree of polarization with model computations for different-sized fractal aggregate particles produced by binary cluster collision aggregation indicate that the radii of the monomers comprising the aggregate particles is near 0.05 μm, almost independent of the number of monomers in the particle.

Haze optical depth and vertical distribution

Before the Huygens probe descent, several workers considered the possibility that the haze in Titan's atmosphere clears below an
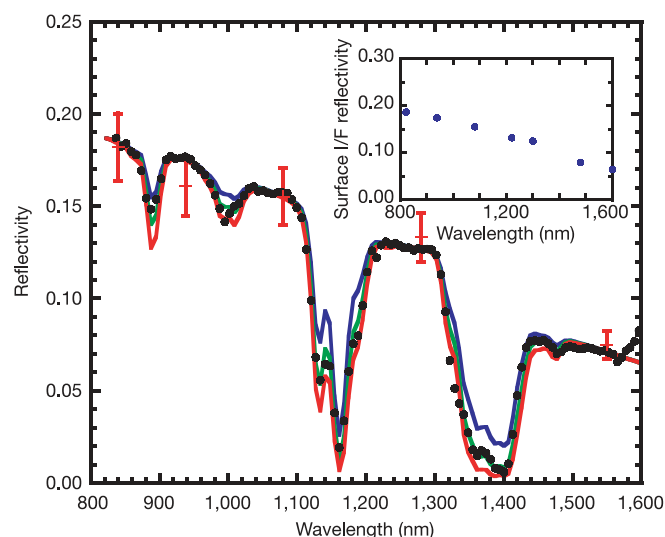

Figure 14 | Derivation of methane mole fraction. Lamp-only downward-looking spectrum from altitude of 21 m (black data points). The red line with three-sigma error bars indicate absolute reflectivity in methane windows estimated from infrared measurements. This spectrum is compared to three models: 3% (blue), 5% (green), and 7% (red) methane mole fractions. These models make use of surface reflectivity at seven wavelengths (shown in inset by the blue points; I/F is the ratio of the intensity to the solar flux divided by π) and linearly interpolated between. From the lamp-on infrared spectra, a lamp-only spectrum at 21 m (representing the spectrum observed by DLIS in the absence of solar illumination) was obtained as follows. First, the reflectivity in regions of negligible methane absorption (at 840, 940, 1070, 1280 and 1,500–1,600 nm) was estimated by the ratio of mean upward intensity (measured by DLIS) to mean downward intensity (measured by ULIS). The mean upward intensity is the average measured over the seven low-altitude DLIS spectra showing no contribution from the lamp (734 to 53 m). The mean downward intensity was obtained by averaging the strongest intensity with the weakest intensity. This average gives reasonable approximation of the downward flux divided by π. The ratio of the mean upward intensity to the mean downward intensity gives reflectivity. Two corrections were required in this analysis: correction for the spatial response of the ULIS diffuser and correction for the solar illumination in the DLIS 21-m spectrum. The correction for diffuser response ranged from 15% (840 nm) to 25% (1,550 nm), assuming a haze optical depth of ~2 at 938 nm. The contribution of solar illumination in the DLIS spectrum at 21 m was eliminated by subtracting the average of the DLIS spectra at 85 and 109 m where the lamp contribution was negligible. The difference spectrum was then divided by the spectral response of the lamp and scaled by a constant to match the continuum reflectivities inferred previously, producing the lamp-only spectrum at 21 m.

Figure 13 | Spectral comparison of bright highlands and dark lowlands. Spectra of the dendritic river highlands and lakebed lowlands areas are compared. To restrict the influence of the atmosphere, only spectra recorded at the same nadir angle are selected. The solid and dashed curves are the average spectra associated with the two spectral pixels outlined in white near the areas marked 'A' (dendritic highlands, solid) and 'B' (dark lakebed, dashed), respectively in Fig. 12. The two pixels bordering 'C' in Fig. 12 yield a spectrum intermediate to the 'A' and 'B' spectra. The spectra have been corrected for albedo by dividing by the total intensity to emphasize the difference in slope. Not shown here is that the reflectivity of the dendritic area ('A') is higher than that of the lakebed area ('B') at all wavelengths by roughly a factor of two. The asterisks denote the methane windows taken for the reddening ratio in Fig. 12.

altitude of some 50 or 70 km (ref. 22) owing to condensation of hydrocarbon gases produced at high altitudes that diffuse to lower, colder, levels of the stratosphere. If such a clearing were to occur in Titan's atmosphere, the intensity seen by the downward-looking DISR spectrometer would be relatively constant below the altitude at which the clearing began.

The brightness looking downward averaged along the DLVS slit and averaged over azimuth increases by a factor of two from the surface to 30 km altitude at a wavelength of 830 nm as shown in Fig. 17a. The increase at 830 nm is due almost solely to scattering by haze between 30 km and the surface. These observations demonstrate that there is significant haze opacity at all altitudes throughout the descent, extending all the way down to the surface.

The brightness of the visible spectra looking upward depends on the azimuth relative to the Sun. Although the probe attitude is not yet well known, it is clear that the minimum intensities are found looking away from the Sun. The upward-looking spectra looking away from the Sun start with low intensities at the highest altitudes and increase in intensity as the altitude decreases from 140 to about 50 km (see Fig. 17b). Below 50 km the intensity decreases at short wavelengths as altitude decreases, while the intensity in continuum regions longer than 700 nm continues to increase, as shown in Fig. 17c.

The intensity looking upward away from the Sun, and the azimuthally averaged intensity looking downward at each continuum wavelength as functions of altitude, constrain the vertical distribution of aerosol opacity in the atmosphere as well as the aerosol single-scattering albedo. With the monomer radius fixed at
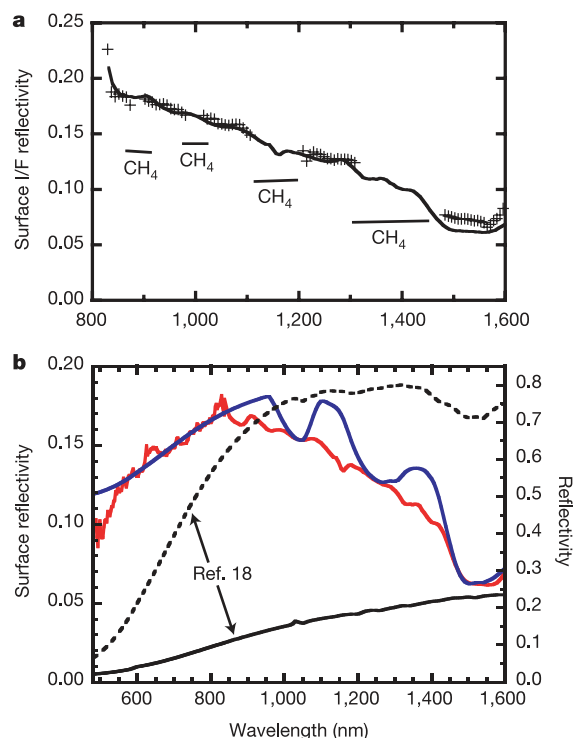
0.05 μm from the polarization measurements, the adjustable parameters include the number of monomers in each aggregate particle, N, as well as the local particle number density, n, in cm^{-3} as a function of altitude. An algorithm developed by (and available from) M.L. was used to determine the single-scattering phase function, the single-scattering albedo, and the extinction cross-section for each aggregate particle as functions of the wavelength, the real and imaginary refractive indices, the monomer radius, and the number of monomers per aggregate particle. This algorithm is based on the discrete dipole approximation and the T-matrix method (M. Lemmon, personal communication) to evaluate the single-scattering properties of the aggregate particles. These computations are most accurate at relatively small particle sizes and depend on extrapolation for N of 256 or larger.

For large particles the wavelength dependence of the extinction optical depth is smaller than for small particles. An N larger than about 100 is required to fit the observations. Hence, models with $N = 256$ or 512 monomers per particle are shown, even though for these values of N the single-scattering algorithm is not as accurate as desired. For these initial models, the real and imaginary refractive indices for the aerosols are taken from the measurements of laboratory tholins in ref. 23.

The radius, R_p, of the circle having the same projected area as an aggregate particle is given by $R_p = r\sqrt{(N^{0.925})}$, where r is the monomer radius and N is the number of monomers. Particles with 256 or 512 monomers have the same projected areas (which control their forward scattering properties) as circles with radii 0.65 and 0.9 μm, respectively.

Comparison of the observed downward-streaming intensity looking away from the Sun at wavelengths of 531 and 829 nm with
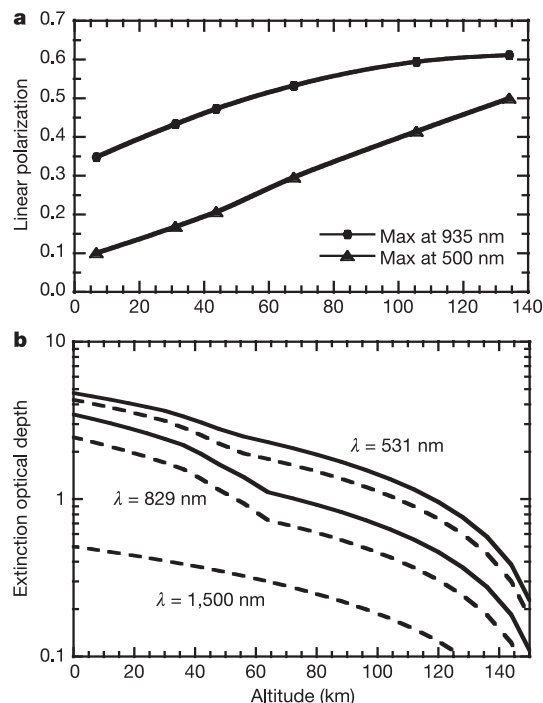

Figure 15 | Reflectance of Titan's surface. a, Reflectivity measured from 21 m altitude ('plus' symbols) compared to the reflectivity after landing (solid curve). The methane absorption bands are indicated by the CH_4 symbol. **b,** Surface reflectivity as measured after landing (red line). It is compared with a simulation (blue line) of a mixture of large-grained (750 μm) low-temperature water ice, yellow tholins, and an unknown component with featureless blue slope between 850 and 1,500 nm. Spectra of two different organic tholins: a yellow tholin (dashed line) and a dark tholin (solid black line) from ref. 18 are also shown for comparison (reflectance scale reduced by a factor of 4). We are attempting to identify or synthesize the missing blue material in our laboratory.

Figure 16 | Haze properties. a, The maximum degree of linear polarization measured opposite to the Sun as a function of altitude in our 500-nm channel (triangles) and in the 935-nm channel (dots). **b,** Extinction optical depth versus altitude for three wavelengths, 531 (top), 829 (middle) and 1,500 nm (bottom). The dashed curves correspond to $N = 256$ monomers, and the solid curves correspond to $N = 512$ monomers of the aggregate particles that make up Titan's haze. Note that the 531 (top) curve was constrained above 40 km and extrapolated to the ground. More explicit constraints from the infrared spectrometer will be available after the probe azimuth with time is determined.

plane-parallel radiative transfer models constrains the vertical distribution of optical depth in Titan's atmosphere. The vertical distribution of particles can be adjusted to fit these curves arbitrarily well. In this preliminary work, only one constant number density
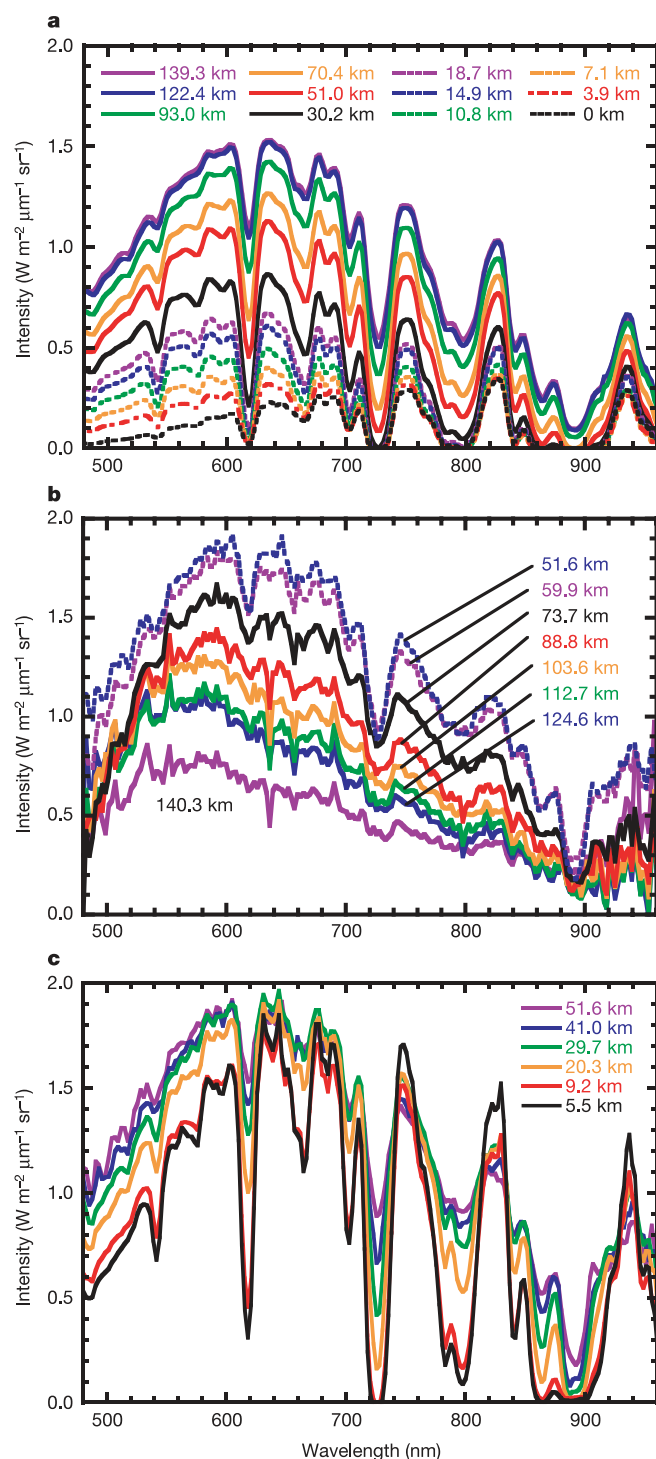
above an altitude of 80 km and a second constant number density below 80 km were considered for models with $N = 256$ and $N = 512$, as shown in Fig. 18a. The number densities are larger in the lower half of the atmosphere than the upper half, but only by modest factors of two to three. The number densities are not exactly equal in the models at different wavelengths, but this is probably due to the extrapolation in the wavelength dependence of the cross-sections in the models for these relatively large N values at the shortest wavelengths (and largest size parameters). Average number densities in the entire atmosphere between 30 and 65 cm^{-3} are required if the number of monomers per particle is 256. Average number densities between 15 and 40 cm^{-3} are required if N is 512.

Figure 17 | Atmospheric spectra. a, The average intensity looking downward averaged over azimuth and over the length of the slit (10° to 50° nadir angle) as a function of wavelength for several altitudes as labelled. **b**, The intensity measured by the Upward-Looking Visible Spectrometer in the direction opposite the Sun as a function of wavelength for several altitudes as labelled. Note that the brightness begins at a low level at 140 km, and increases as altitude decreases. **c**, Same as **b** but for altitudes below 50 km. Note that the brightness away from the Sun decreases with decreasing altitude at short wavelengths, but increases in continuum regions longward of 700 nm.
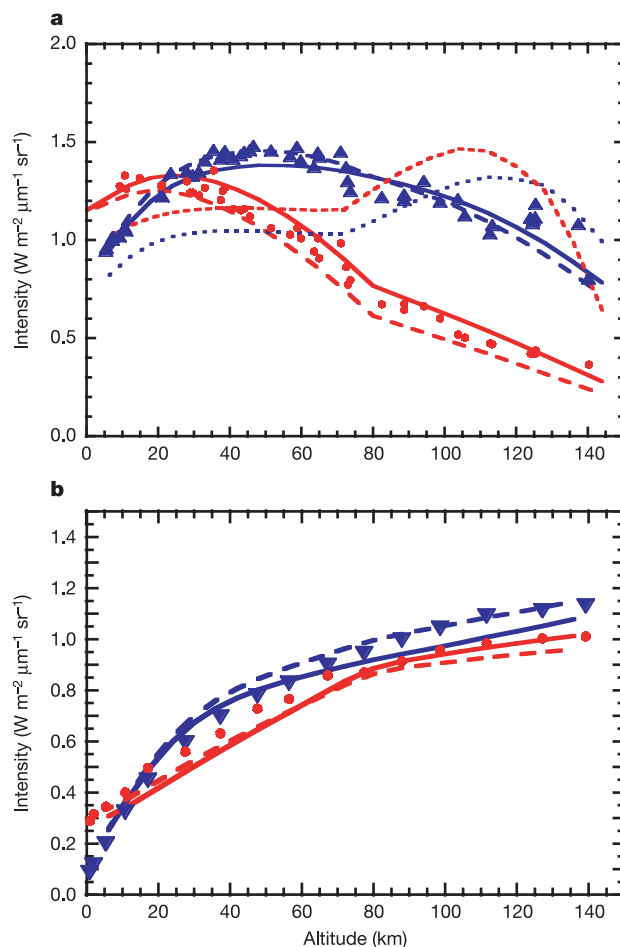

Figure 18 | Haze models versus observations. a, Measured upward-looking intensity (points) away from the Sun versus altitude for 531 (blue) and 829 nm (red). Three models are shown compared to the observations at each wavelength. The solid curves are for 512 monomers in each aggregate particle. The model at 531 nm has 12 particles cm^{-3} above 80 km and 18 particles cm^{-3} below that altitude. The corresponding model at 829 nm has 20 particles cm^{-3} above 80 km and 60 cm^{-3} below. The models indicated by long-dashed lines have 256 monomers per particle and at 531 nm the number density is 20 particles cm^{-3} above 80 km and 40 cm^{-3} below. At 829 nm the number density is 30 cm^{-3} above 80 km and 100 cm^{-3} below. The number density of particles differs slightly with wavelength because the model of fractal aggregate particles does not yet reproduce the wavelength dependence of the cross-section to high accuracy. The models indicated by short-dashed lines have 256 monomers per particle, and have the same number of total particles as the models indicated by long-dashed lines, but all the particles are concentrated above 72 km with a clear space below. Such models with clear spaces are clearly not in agreement with the observations. **b**, Downward-looking measured intensities versus altitude (plotted as points) for 531 (blue points) and 829 nm (red points). The two models (plotted as curves) are the same models as those shown by long-dashed lines and solid curves in **a**.

Models with a clear space below an altitude of 72 km are also shown in Fig. 18a. It is apparent that no such clear space exists in the region of the probe's entry. It will be interesting to examine the range of parameters in cloud physics models needed to reproduce the continuous variation of haze opacity throughout Titan's atmosphere.

Haze models must reproduce the upward-streaming intensity observed in the atmosphere as well as the downward-streaming intensity. Models with $N = 256$ and 512 at 531 and 829 nm are compared to the upward intensity averaged in azimuth and along the slit in Fig. 18b. While the fit is not exact, it is clear that the models that fit the downward intensity away from the Sun are also in reasonable agreement with the measured upward intensities. It is interesting to note the ground reflectivity implied by the measurements at 531 and 829 nm. These values include the true shape of the diffuser in the Upward-Looking Visible Spectrometer and produce ground reflectivities of 0.13 at 531 nm and 0.19 at 829 nm. The corrected value at 829 nm is in good agreement with the value measured by the Infrared Spectrometer (0.18) when a correction for the diffuser's non-ideal shape is made to the infrared spectrometer measurements.

Haze structure and methane absorptions

Haze models must fit the observations at all wavelengths. How well do the models derived from the visible spectrometer fit the DISR observations in the infrared? The ULIS spectra in Fig. 19 clearly show absorption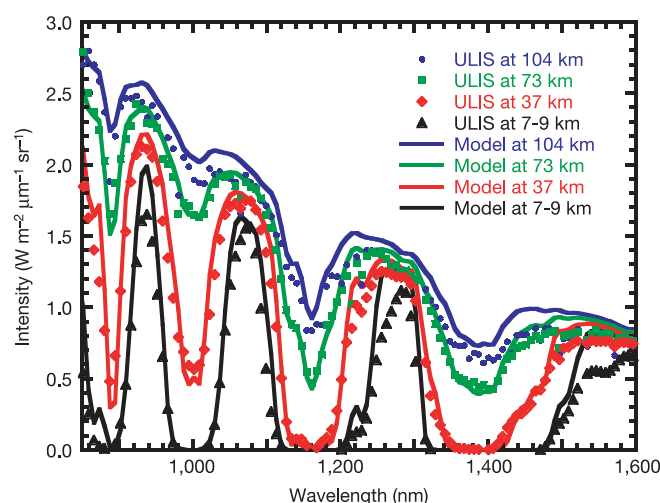 by the methane bands around 890, 1,000, 1,160 and 1,380 nm. The depths of these bands increase with decreasing altitude as a result of increasing methane column density. They are correctly reproduced by radiative transfer calculations based on an exponential sum formulation for the methane absorption and a stratospheric methane mole fraction of 1.6% (ref. 24). The agreement is worse at low altitudes in the troposphere, probably owing to inaccuracies in the methane absorption coefficients. In the methane windows the downward average intensity varies by 25% or less between 104 and 10 km, indicating relatively low aerosol absorption in the infrared range.

At altitudes less than 3.5 km, we used single short exposures for the infrared spectra rather than long time averages. The 940 nm intensity in the last three ULIS spectra is about four times larger that in the first three spectra, indicating that the Sun is located in their field of view (see Fig. 20). The contrast between the most intense spectrum (with the Sun in the field of view) and the weakest one (with the Sun out of the field of view) increases with wavelength, reaching 17 at 1,550 nm, a consequence of the decreasing haze optical depth. This contrast can be used to constrain the haze optical depth, assuming that the spectra correspond approximately to solar azimuths of 0 and 180°. A satisfactory model, using aggregate particles of 256 monomers, a 0.05-μm monomer radius, and a uniform concentration of 52 particles cm^{-3}, indicates an optical depth of about 2 at 940 nm, decreasing to 0.5 at 1,550 nm. Models with one-half and twice the particle density (and hence optical depth) yield a contrast between spectra with the Sun in and out of the field about twice as large and half as large (respectively) as observed.

The methane bands are prominent in the DLIS spectra at all altitudes (see Fig. 21a). The residual intensity in the cores of these bands is due to scattering by aerosol particles between the probe and the surface. Its variation provides a constraint of the vertical profile of the haze particles between approximately 150 and 40 km, as illustrated in Fig. 21a. The method is not sensitive at low altitudes because of absorption of the downward solar flux in the methane bands. A model with a constant particle concentration with altitude provides a
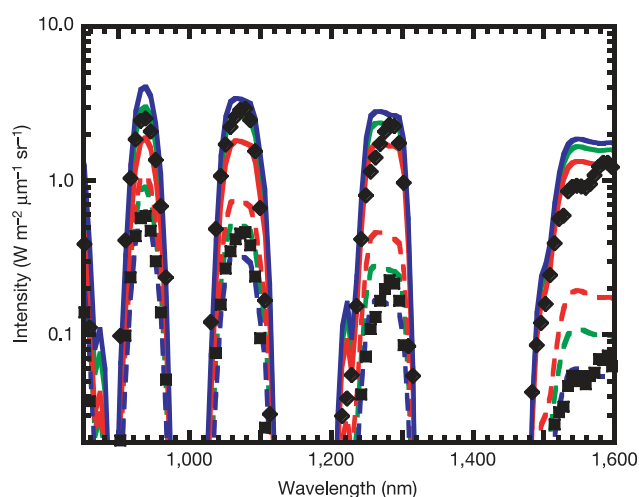

Figure 19 | Vanishing sunlight. ULIS spectra (points) recorded at various altitudes and showing the growth of the methane-band absorption with depth in the atmosphere. The spectra at altitudes greater than 3.5 km have been integrated over several probe rotations and correspond approximately (but not exactly) to azimuth-averaged intensities. The full analysis of these observations must await refinement of the attitude of the probe as a function of time, a task still in progress. Models, with a methane mole fraction of 1.6% in the stratosphere increasing to 5% at the surface, are shown for comparison (lines). At low altitudes (<20 km), the mismatch between model and observations in the methane windows, specifically around 1,280 and 1,520–1,600 nm, is probably due to errors in the methane absorption coefficients at long path-lengths. The model slightly overestimates the intensity in the 104-km spectrum, because the latter does not correspond to an exact azimuth average. Radiative transfer calculations were based on a 16-term exponential-sum formulation of the methane absorption properties. In the near-infrared ($\lambda > 1,050$ nm), these absorption coefficients were calculated from a band model with a modified temperature dependence designed to better match the low-temperature observations. In the visible ($\lambda < 1,050$ nm), the absorption coefficients of Karkoschka[34] were used. In practice, for 30 pressure–temperature conditions representative of 30 levels in Titan's atmosphere[12], methane transmissions were calculated for 60 different paths, convolved to the resolution of the DISR spectrometers, and this ensemble of convolved transmissions was fitted each time with an exponential-sum model.

Figure 20 | Determination of total haze optical depth. ULIS spectra (black points) recorded at 734 m (diamonds) and 53 m (squares) above the surface with integration times of 1 s. The one with the highest intensity (734 m) has the Sun in its field of view; the lower one (53 m) does not. The contrast between the two in the methane windows increases with wavelength and is a sensitive function of the haze optical depth. The nominal model, shown for comparison (green line), has an optical depth of 2 at 940 nm decreasing to 0.5 at 1,550 nm. Calculations correspond to intensities averaged over the field of view and azimuths of 0 and 180 degrees with respect to the Sun. Other models show the effect of doubling (red) and halving (blue) the particle concentration. Solid lines show model intensity towards the Sun while the dashed lines show the intensity with the instrument facing away from the Sun.

good fit of the methane bands. Moderate variations of the particle concentration with height are also acceptable, but a model with a clear space in the lower stratosphere is inconsistent with the data.

The optical depths in the models that fit the visible and infrared spectral observations with $N = 256$ and 512 are shown as functions of altitude in Fig. 16b. The number density was assumed to be $52 \, cm^{-3}$, independent of altitude for the infrared models with $N = 256$. The models computed for comparison with the visible spectrometer contained constant and different number densities above and below 80 km. The average number density above and below 80 km for the models with $N = 256$ (30 and 65) are in reasonable agreement with the single value used in the models derived from the infrared spectrometer. The same particle number densities give the required optical depths from 900 to 1,550 nm, indicating that the algorithm for generating cross-sections from particle sizes is working in a consistent manner. At shorter wavelengths (531 nm), the size parameter is sufficiently large that the

cross-section algorithm is not as accurate, and the number density is decreased slightly to give models that fit the observations. The variation of optical depth with wavelength is modest, decreasing by only about a factor of 2.8 from 500 to 1,000 nm. If 512 monomers are used for the particles, the wavelength dependence is even less steep. The haze optical depth as a function of wavelength is presented in Fig. 21b.

A thin layer of haze near 21 km altitude

Many workers have suggested that hydrocarbons produced at very high altitudes could diffuse downward to cooler levels where they could condense on haze particles. Do our intensity profiles looking towards the horizon detect any thin haze layers at specific altitudes that might be due to this mechanism?

Figure 22 shows the normalized profile of intensity measured by the Side-Looking Imager (SLI) compared to a model. The left-hand side of the plot shows normalized intensity as a function of nadir angle for the observations at altitudes ranging from 20.4 to 22.3 km. The observations at 22.1 km and above and at 20.4 km and below show smooth functions of nadir angle. However, for the measurement at 20.8, and the two measurements at 20.9 km altitude, a dip of about 2% is seen near a nadir angle of 90°.

The curves in the right-hand side of Fig. 22 show the intensities of a model having a thin additional layer of haze at an altitude of 20.9 km. The haze layer of vertical absorption optical depth within a factor of two of 0.001 with a gaussian profile between 1 and 2 km thick can reproduce the depth of the feature. The location of the layer is at $21.0 \pm 0.5 \, km$, where the local temperature is 76 K and the pressure is 450 mbar (ref. 12).

This feature at 21 km occurs in the troposphere and may be an indication of methane condensation. It is the only indication of a thin layer seen in the set of SLI images taken from 150 km to the surface. Evidence of condensation of hydrocarbons in the lower stratosphere, where several hydrocarbons might be expected to condense[25], has not yet been found, but the search is continuing.

Unravelling Titan's mysteries

Some of the major questions about Titan concern the nature of the source of methane that replaces the irreversible loss at high
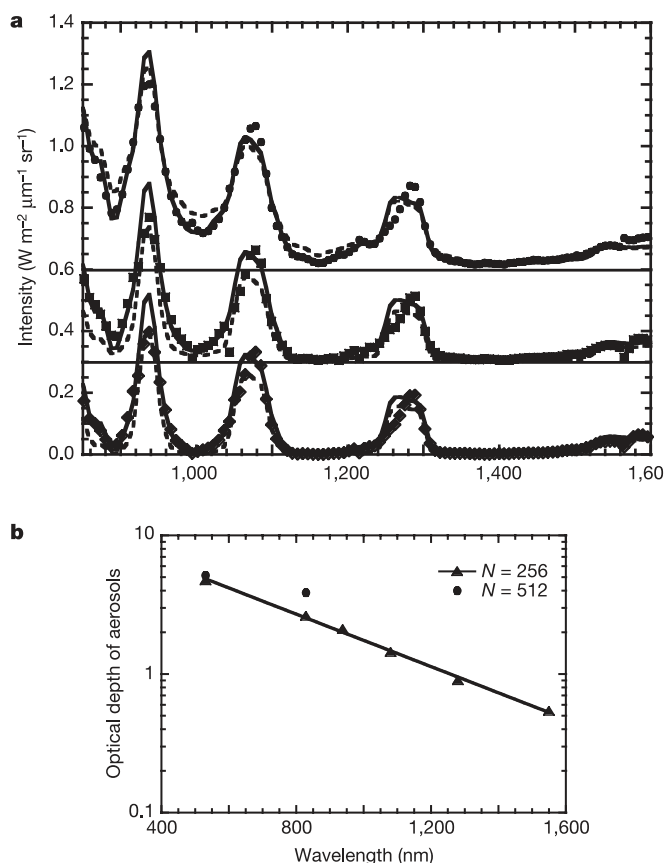
Figure 21 | **Haze vertical structure and total optical depth. a,** DLIS spectra recorded at three altitudes: 104 km (top, dots), 82 km (middle, squares), and 57 km (bottom, diamonds). The intensities for the higher altitudes have been displaced in 0.3 increments for clarity. The points are measured data; the lines are the nominal model; the dashed lines are a modified model with the same optical depth as the nominal model, but with all the haze particles concentrated above 72 km (clearing below). The residual intensity in the core of the methane bands is a sensitive indicator of the presence of scattering particles beneath the probe. The model with the clearing produces too much emission in the core of the CH_4 bands at high altitude and not enough at low altitude. **b,** Total extinction optical depth of the haze alone versus wavelength. The triangles are for models with 256 monomers per particle. The points at the two shortest wavelengths are from models that fit the visible spectrometer measurements. The other four points are from models that fit the infrared spectrometer measurements. The dots are for models with 512 monomers per particle that fit the visible spectrometer measurements.
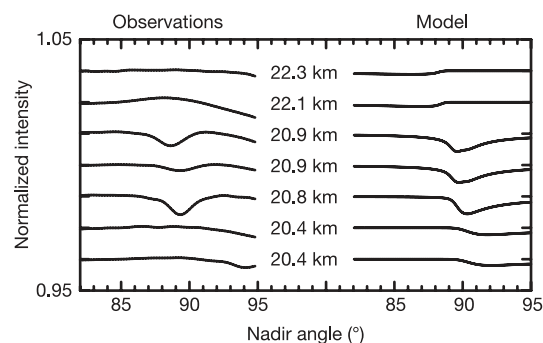
Figure 22 | **Thin cloud layer observation at 21 km.** In the left-hand side are the intensity profiles as a function of nadir angle divided by the average intensity profile measured by the SLI at the altitudes indicated. The right-hand side of the figure shows the model intensity profiles computed for a cloud layer of absorption optical depth 0.001 which is 1 km thick at an altitude of 21 km. The model is able to reproduce the 2% contrast feature seen in the observations at altitudes of 20.8 and 20.9 km. If the layer is mostly illuminated by diffuse light, the absorption optical depth is equal to total optical depth times the difference between the single-scattering albedos of the material in the layer and the albedo of the background haze. If the layer is primarily illuminated by direct sunlight, the absorption optical depth of the haze is proportional to the total optical depth of the haze times the difference between the phase functions of the material in the layer and the background haze at the scattering angles for any observation.

altitudes by photochemistry that produces a host of complex organic compounds. Open pools of liquid hydrocarbons on the surface have been suggested, as well as cryovolcanism. Also, if methane photochemistry has been occurring over the lifetime of the Solar System the organic products of these processes should have accumulated to significant depths on the surface and should be seen in images and spectra of the surface.

Although no such liquid bodies were directly imaged by DISR, there is compelling evidence for fluid flow on the surface of Titan, including the dendritic and stubby drainage channel networks, the rounded and size-graded 'rocks' at the surface landing site, and the morphology of the shoreline, offshore structures, and the appearance of the darker lakebed region. The stubby networks may imply sapping or spring-fed flows, as the existence of liquid pools on the surface and the frequency of precipitation that could cause the deep dendritic drainage channels are both still unconfirmed. In addition, there are at least a few structures that suggest cryovolcanic flows on the surface.

The ground track derived by the image correlations demonstrates a zonal wind field that is mostly prograde. The general altitude profile and shape agree with predicted average models of the zonal wind flow between 50 and 10 km altitude[7], although with a reduced intensity. Below 10 km, falling wind speeds and an abrupt change of wind direction indicate a planetary boundary layer some 7–8 km thick, scaling nicely from near-equatorial terrestrial boundary layers.

Spatially resolved spectral reflectance measurements of different regions on the surface suggest that the uplands are redder than the lowland lakebed regions. The regions near the mouths of the rivers are also redder than the lake regions. A host of questions about the sequence of flooding and formation of these structures is suggested by these observations.

The reflectivity of the surface at the landing site was measured from 480 nm to 1,600 nm without the interference of methane absorption bands or haze opacity. The peak reflectivity in the dark regions is about 0.18 at 830 nm and decreases towards longer and shorter wavelengths. The red slope in the visible is consistent with organic material, such as tholins, but the blue infrared slope is still unexplained. Between 1,500 and 1,600 nm the reflectivity is low (0.06) and flat, consistent with water ice. Nevertheless, the decrease in reflectivity from 900 to 1,500 nm does not show the expected weak absorption bands of water ice near 1,000 and 1,200 nm, and the identity of the surface component responsible for this blue slope remains unknown.

The nature of the haze aerosols measured by DISR is different in significant ways from the view before the Huygens mission. Before the Huygens probe, cloud physics models with sedimentation and coagulation predicted a strong increase in haze density with decreasing altitude[9]. In addition, measurements of the high degree of linear polarization in light scattered from Titan near a phase angle of 90° by the Pioneer and Voyager spacecraft could only be matched by spherical particles having radii less than or equal to 0.1 μm. Such small particles produced a strong increase in optical depth with decreasing wavelength shortward of 1,000 nm. Fitting the strong methane band at 890 nm constrained the amount of haze at high altitudes. This haze became optically much thicker at the wavelength of the weaker methane band at 619 nm. To fit the observed strength of this band it was necessary to remove the haze permitted by the cloud physics calculations at altitudes below about 70 km by invoking condensation of organic gases produced at very high altitudes as they diffused down to colder levels[26]. The condensation of many organic gases produced by photochemistry at high altitudes on Titan was suggested by Sagan and Thompson in ref. 25, and seemed consistent with this view.

The next development in Titan haze models (pioneered by R.W., P.S., Cabane, M. and M.L.) included the use of fractal aggregate haze particles that had a small component (monomer) with a radius of about 0.06 μm to produce strong linear polarization[26–30]. These monomers stuck together in an aggregation of many tens (or more) monomers. The large size of the aggregation could produce the strong forward scattering required from the Titan haze aerosols while preserving the high degree of linear polarization. However, it was quite laborious to compute the single-scattering properties of such aggregate particles for more than about 100 monomers at visible wavelengths. Particles with an effective radius of about 0.35 μm were required to produce the degree of forward scattering observed by Voyager[31]. This required the number of monomers in an aggregate particle to be about 45, and permitted single-scattering computations of the cross-section and phase function of the particles over the visible range. Of course, even larger numbers of monomers per particle would have matched the observations at high phase angles on Voyager, but these were difficult to perform and have largely gone unexplored. If larger particles had been used, however, the optical depth of the aerosols at shorter wavelengths would not have been nearly so large, and the clear space below 70 km may well not have been necessary.

The new DISR observations give a measurement of the monomer radius of 0.05 μm, in good agreement with previous estimates. Significantly, however, they show that the haze optical depth varies from about 2 at 935 nm to only about 4.5 at 531 nm, and the number of monomers in a haze particle is therefore probably several hundred. A value of 256 for N gives a projected area equal to that of a sphere of radius 0.65 μm, about twice as large as previously assumed. With $N = 512$, the equivalent sphere with the same projected area has a radius of 0.9 μm, nearly three times the size previously used. In any case, it seems that the size of the aggregate particles is several times as large as in some of the older models. A better estimate of the particle size will be available after the analysis of the solar aureole measurements of the variation in brightness near the Sun. In addition, measurements by the DISR violet photometer will extend the optical measurements of the haze to wavelengths as short as the band from 350 to 480 nm, also helping to constrain the size of the haze particles.

The number density of the haze particles does not increase with depth nearly as dramatically as predicted by the older cloud physics models. In fact, the number density increases by only a factor of a few over the altitude range from 150 km to the surface. This implies that vertical mixing is much less than had been assumed in the older models where the particles are distributed approximately as the gas is with altitude. In any case, no clear space at low altitudes, which was suggested earlier[32], was seen.

The methane mole fraction of 1.6% measured in the stratosphere by the Composite Infrared Spectrometer (CIRS) and the Gas Chromatograph Mass Spectrometer is consistent with the DISR spectral measurements. At very low altitudes (20 m) DISR measured 5 ± 1% for the methane mole fraction.

Finally, the entire set of DISR observations gives a new view of Titan, and reinforces the view that processes on Titan's surface are more similar to those on the surface of the Earth than anywhere else in the Solar System.

1. Coustenis, A. et al. Maps of Titan's surface from 1 to 2.5 μm. Icarus 177, 89–105 (2005).
2. Porco, C. C. et al. Imaging of Titan from the Cassini spacecraft. Nature 434, 159–168 (2005).
3. Sotin, C. et al. Infrared images of Titan. Nature 435, 786–789 (2005).
4. Elachi, C. et al. Cassini radar views the surface of Titan. Science 308, 970–974 (2005).
5. Tomasko, M. G. et al. The Descent Imager/Spectral Radiometer (DISR) experiment on the Huygens entry probe of Titan. Space Sci. Rev. 104, 469–551 (2002).
6. Ivanov, B. A., Basilevski, A. T. & Neukem, G. Atmospheric entry of large meteoroids: implication to Titan. Planet. Space Sci. 45, 993–1007 (1997).
7. Flasar, F. M., Allison, M. D. & Lunine, J. I. Titan zonal wind model. ESA Publ. SP-1177, 287–298 (1997).

8. Bond, N. A. Observations of planetary boundary-layer structure in the eastern equatorial Pacific. *J. Atmos. Sci.* **5**, 699–706 (1992).
9. Lindal, G. F., Wood, G. E., Hotz, H. B. & Sweetnam, D. N. The atmosphere of Titan: An analysis of the Voyager 1 radio occultation measurements. *Icarus* **53**, 348–363 (1983).
10. Tokano, T. & Neubauer, F. M. Tidal winds on Titan caused by Saturn. *Icarus* **158**, 499–515 (2002).
11. Niemann, H. B. *et al.* The abundances of constituents of Titan's atmosphere from the GCMS instrument on the Huygens probe. *Nature* doi:10.1038/nature04122 (this issue).
12. Fulchignoni, M. *et al. In situ* measurements of the physical characteristics of Titan's environment. *Nature* doi:10.1038/nature04314 (this issue).
13. Brown, G. N. Jr & Ziegler, W. T. in *Advances in Cryogenic Engineering* (ed. Timmerhaus, K. D.) Vol. 25, 662–670 (Plenum, New York, 1980).
14. Griffith, C. A., Owen, T., Geballe, T. R., Rayner, J. & Rannou, P. Evidence for the exposure of water ice on Titan's surface. *Science* **300**, 628–630 (2003).
15. Coustenis, A., Lellouch, E., Maillard, J.-P. & McKay, C. P. Titan's surface: composition and variability from the near-infrared albedo. *Icarus* **118**, 87–104 (1995).
16. Lellouch, E., Schmitt, B., Coustenis, A. & Cuby, J.-G. Titan's 5-um lightcurve. *Icarus* **168**, 204–209 (2004).
17. Grundy, W. & Schmitt, B. The temperature-dependent near-infrared absorption spectrum of hexagonal H_2O ice. *J. Geophys. Res. E* **103**, 25809–25822 (1998).
18. Bernard, J.-M. *et al.* Evidence for chemical variations at the micrometric scale of Titan's tholins: Implications for analysing Cassini-Huygens data. *Icarus* (submitted).
19. Coll, P. *et al.* Experimental laboratory simulation of Titan's atmosphere: aerosols and gas phase. *Planet. Space Sci.* **47**, 1331–1340 (1999).
20. Bernard, J.-M. *et al.* Experimental simulation of Titan's atmosphere: detection of ammonia and ethylene oxide. *Planet. Space Sci.* **51**, 1003–1011 (2003).
21. Moroz, L. V., Arnold, G., Korochantsev, A. V. & Wäsch, R. Natural solid bitumens as possible analogs for cometary and asteroid organics. 1. Reflectance spectroscopy of pure bitumens. *Icarus* **134**, 253–268 (1998).
22. Toon, O. B., McKay, C. P., Griffith, C. A. & Turco, R. P. A physical model of Titan's aerosols. *Icarus* **95**, 24–53 (1992).
23. Khare, B. N. *et al.* Optical constants of organic tholins produced in a simulated Titanian atmosphere—From soft X-ray to microwave frequencies. *Icarus* **60**, 127–137 (1984).
24. Flasar, F. M. *et al.* Titan's atmospheric temperatures, winds, and composition. *Science* **308**, 975–978 (2005).
25. Sagan, C. & Thompson, W. R. Production and condensation of organic gases in the atmosphere of Titan. *Icarus* **59**, 133–161 (1984).
26. Lemmon, M. T. *Properties of Titan's Haze and Surface.* PhD dissertation, (Univ. Arizona, 1994).
27. West, R. A. & Smith, P. H. Evidence for aggregate particles in the atmospheres of Titan and Jupiter. *Icarus* **90**, 330–333 (1991).
28. Cabane, M., Chassefière, E. & Israel, G. Formation and growth of photochemical aerosols in Titan's atmosphere. *Icarus* **96**, 176–189 (1992).
29. Cabane, M., Rannou, P., Chassefière, E. & Israel, G. Fractal aggregates in Titan's atmosphere. *Planet. Space Sci.* **41**, 257–267 (1993).
30. West, R. A. Optical properties of aggregate particles whose outer diameter is comparable to the wavelength. *Appl. Opt.* **30**, 5316–5324 (1991).
31. Rages, K. B. & Pollack, J. Vertical distribution of scattering hazes in Titan's upper atmosphere. *Icarus* **55**, 50–62 (1983).
32. McKay, C. P. *et al.* Physical properties of the organic aerosols and clouds on Titan. *Planet. Space Sci.* **49**, 79–99 (2001).
33. Bird, M. K. *et al.* The vertical profile of winds on Titan. *Nature* doi:10.1038/nature04060 (this issue).
34. Karkoschka, E. Methane, ammonia, and temperature measurements of the Jovian planets and Titan from CCD-spectrophotometry. *Icarus* **133**, 134–146 (1998).